NEUTRON SOURCES AND THEIR CHARACTERISTICS*

R. C. McCall and W. P. Swanson
Stanford Linear Accelerator Center
Stanford University, Stanford, California 94305

The significant sources of photoneutrons within a linear-accelerator treatment head are identified and absolute estimates of neutron production per treatment dose are given for typical components. It is found that the high-Z materials within the treatment head do not significantly alter the neutron fluence but do substantially reduce the average energy of the transmitted spectrum. Reflection of neutrons from the concrete treatment room contribute to the neutron fluence, but not substantially to the patient integral dose, because of a further reduction in average energy. The ratio of maximum fluence to the treatment dose at the same distance is given as a function of electron energy. This ratio rises with energy to an almost constant value of 2.1×10^5 neutrons cm^{-2} rad^{-1} at electron energies above about 25 MeV. Measured data obtained at a variety of accelerator installations are presented and compared with these calculations. Reasons for apparent deviations are suggested. Absolute depth-dose and depth-dose-equivalent distributions for realistic neutron spectra that occur at therapy installations are calculated, and a rapid falloff with depth is found. The ratio of neutron integral absorbed dose to leakage photon absorbed dose is estimated to be 0.04 and 0.2 for 14 and 25 MeV incident electron energy, respectively. Possible reasons are given for lesser neutron production from betatrons than from linear accelerators. Possible ways in which neutron production can be reduced are discussed.

Introduction

The radiation field around a medical therapy electron accelerator is a complicated mixture of photons leaking from the head, scattered photons from the patient, beam stopper and room walls, and photons from electrons stopped elsewhere than the target. If the accelerator energy is high enough to produce neutrons, i.e., greater than about 10 MeV, there is also a neutron component. This paper is primarily concerned with the generation and propagation of this neutron field.

Neutron Production

The primary production of neutrons is through (γ,n) reactions with smaller quantities produced by (γ,pn) and $(\gamma,2n)$ if the energy is high enough. The direct production of neutrons by electrons, (e,n), is smaller by about two orders of magnitude -- the fine structure constant modified by several other factors -- and can be neglected. Medical electron accelerators at present are limited to energies less than 45 MeV and our discussion will be limited to that energy range. In this energy domain, neutron production is due to the "giant photonuclear resonance", more commonly called the "giant resonance". The cross section for the giant resonance is characterized by a threshold energy, a rapid rise to a prominent peak and a more gradual decrease at higher energies. For the medium and heavy nuclei (A > 40) which are of interest to us, the peak occurs at 13-18 MeV. Threshold energies for some materials of interest are listed in Table I. A recent compilation of threshold energies has been published by Howerton.[4] A recent and comprehensive set of photoneutron cross sections is by Berman.[2]

Table I. Thresholds of Photoneutron Reactions.

Element	Atomic Number	Abundance (Percent)	(γ,n) Threshold Energy (MeV)
Pb	206	25.1	8.08
	207	21.7	6.74
	208	52.3	7.37
Fe	54	5.8	13.4
	56	91.7	11.2
W	182	26.4	8.05
	183	14.4	6.19
	184	30.6	7.41
	186	28.4	5.75

The yield of photoneutrons is proportional to the convolution of the (γ,n) cross section and the bremsstrahlung spectrum, which decreases rapidly with photon energy. The result is a yield curve which increases rapidly with primary electron energies for constant electron current up to approximately 25 MeV and more slowly thereafter. For constant electron beam power, the neutron yield is almost constant with primary electron energy above 35 MeV. Swanson[16] has recently published electron yield calculations applicable to this energy range.

Neutron spectra in the giant resonance contain two components -- the evaporation spectrum and the direct emission spectrum. The evaporation spectrum is the larger component and can usually be described adequately by a Maxwellian distribution

$$\frac{dN}{dE_n} = \frac{E_n}{T^2} \exp\left(\frac{-E_n}{T}\right)$$

To be presented at the Conference on Neutrons from Electron Accelerators, Gaitherburg, Maryland, April 9 - 10, 1979.

where T is the nuclear "temperature" in MeV for the particular nucleus and is also a function of the excitation energy. One should note that the spectrum peaks at $\hat{E}_n = T$ (most probable energy) and has an average energy of $\bar{E}_n = 2T$. The evaporation neutrons are emitted almost isotropically.

The direct emission neutrons tend to be higher energy than the evaporation neutrons and may be emitted nonisotropically. Mutchler[8] found that for medium to high atomic number materials and energies near the resonance peak, direct emission amounted to about 14% of the total neutrons. Figure 1[9] shows typical photoneutron spectra with the direct emission neutrons responsible for the "bump" on the high-energy side of the spectrum. For comparison a fission neutron spectrum is also shown in Fig. 1.
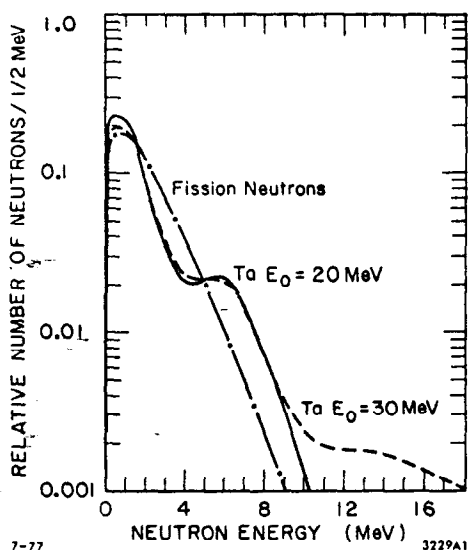
Fig. 1. Photoneutron spectra for Ta with peak bremsstrahlung energies of 20 and 30 MeV, compared to a fission spectrum. From NBS-97.[9]

It will be shown later that the spectrum of photoneutrons can be degraded rapidly in heavy metals so published spectra must be considered as representative of a particular target thickness.

Transport of Neutrons in the Treatment Head

The typical medical accelerator has massive shielding around the target to provide photon shielding and produce a collimated beam of x-rays. Neutrons which are produced inside the head are produced approximately isotropically and penetrate the head shielding in all directions. The photon shielding is usually of some heavy metal such as tungsten or lead, and there is also a certain amount of iron and copper from bending magnets in the head. These materials provide some photon shielding action since these are all heavy elements. The only significant neutron energy loss mechanisms in these heavy elements are inelastic scattering or (n,2n) reactions. Both of these processes are effective in the MeV energy region

but the (n,2n) reaction is most effective at the higher energies. Inelastic scattering can occur only at energies above the lowest excited state of the shielding material. These lowest excited states are in the neighborhood of 0.6 to 0.8 MeV for lead and iron but about 0.1 MeV for tungsten; therefore tungsten is more effective in reducing the energy of neutrons by inelastic scattering. The energy loss in any inelastic collision cannot be exactly determined or predicted, but there is a minimum energy loss equal to the energy of the lowest excited state. Often there is large energy loss in a single collision resulting in excitation of higher energy states followed by a cascade of gammas. In the (n,2n) reaction the minimum energy loss is equal to the binding energy of a neutron, and since the energies of two emerging neutrons tend to be similar, they produce large numbers of quite low energy neutrons. The total of the inelastic plus (n,2n) cross sections is of the order of 1 or 2 barns for these materials. This means that the typical neutron penetrating the photon shielding undergoes several collisions. In addition, a large amount of elastic scattering takes place in these materials at these energies. The elastic scattering results in negligible energy loss but does, however, have the effect of lengthening the path length for the neutrons in the shielding material and offering greater opportunity for the inelastic and (n,2n) reactions to occur. The attenuation of neutron fluence is small, however, since the capture cross sections of these materials are small down to thermal energies. With a spectrum containing high-energy neutrons, such as a fission or PuBe spectrum, there can, in fact, be a slight buildup of neutron fluence due to the (n,2n) reactions.

In a previous paper[6] hereafter referred to as MJS, the Monte Carlo computer program MORSE[14] was used to explore the effects of the head shielding on several photoneutron spectra. It was shown that while there is very little attenuation of neutrons by lead and iron, there is some attenuation by tungsten amounting to about 15% in the typical therapy machine shielding. It was also shown that the dose equivalent is attenuated by the shielding because of the reduced energy of the spectrum. In the course of the calculations in MJS, it was found that the average energy of a neutron spectrum is a very useful parameter for studies around radiotherapy machines. Figure 2, taken from MJS, shows the fluence-to-dose-equivalent conversion factor for a neutron spectrum with average energy $\bar{E}$, plotted against $\bar{E}$. It is seen that these data can be fit with a straight line which is almost parallel to the curve (labeled ICRP-21 in Fig. 2) drawn through the points listed in ICRP-21[5] for the conversion of monoenergetic neutron fluences to dose equivalent. It should be kept in mind that these conversion factors from ICRP-21 are calculated at the depths where the dose equivalent is maximum. For a spectrum, each energy component has it's maximum does-equivalent at a different depth, so a simple addition of dose-equivalent components will result in an overestimate. The estimates of Fig. 2 are slight overestimates for this reason. However, it will be shown that the average neutron energies around medical accelerators are so low that this is probably not significant. In Figs. 3 and 4 are shown the average energy of several
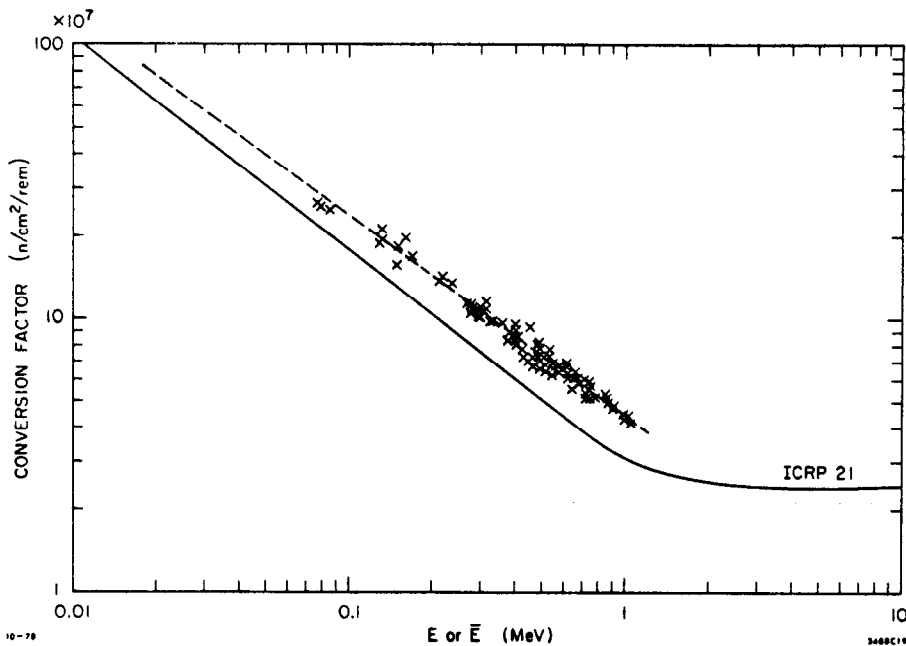
Fig. 2. Factor for converting dose-equivalent to neutron fluence. The curve is based on recommendations of ICRP-21[5] and is a function of mono-energetic neutron energy. The x's are the result of averaging the ICRP-21 conversion factor over spectra from a large variety of sources, and are presented as a function of average neutron energy. The dashed line is a least squares fit which is nearly parallel to the ICRP monoenergetic values.

spectra calculated after passing through various thicknesses of tungsten and lead.[6] It can be seen that tungsten reduces the average energy faster than lead, and also that this reduction continues out to greater depths. After a certain thickness, of any material, virtually all of the neutrons will have their energy reduced below the lowest excited state, and inelastic scattering can no longer occur. This is well below the (n,2n) threshold. Thereafter, the neutrons penetrate for very large distances through these heavy metals with no further attenuation or decrease in dose equivalent.
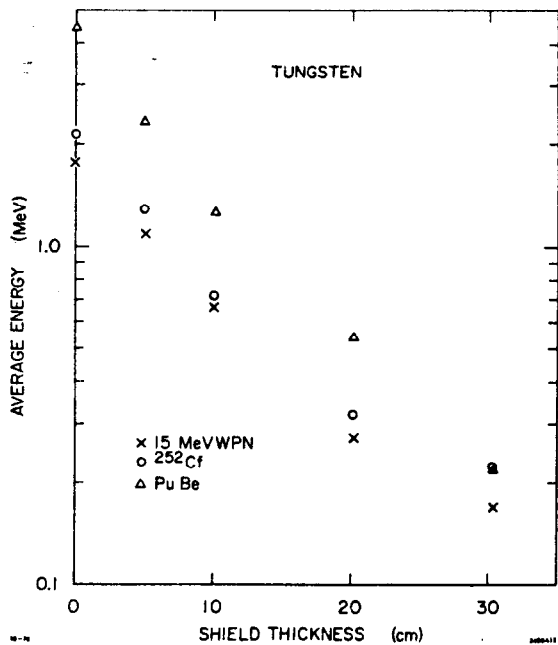

Fig. 3. Calculated average neutron energy as a function of W thickness for 15 MeV (incident electron energy) photoneutrons, and ^{252}Cf and PuBe neutron spectra. Over the range of W thickness typically used, there is a substantial decrease in average neutron energy in penetrating the head shielding. Data are from the Monte-Carlo program MORSE.
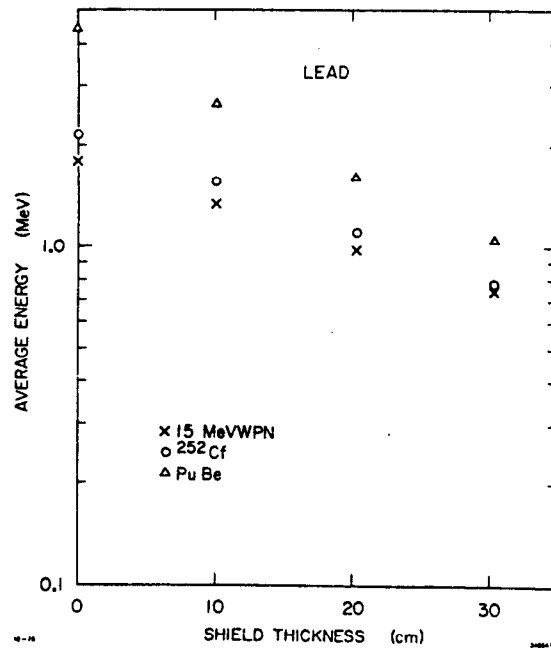

Fig. 4. As for Fig. 3 but for Pb. The reduction in average neutron energy is somewhat less for Pb than for W, even when the two materials are compared on an areal-density basis.

It is frequently stated that a fission spectrum is very similar to the photoneutron spectrum found in machines in this energy range. This is true for the primary spectra, but not for the spectra after they have penetrated the head shielding. In Fig. 5, we show the integral photoneutron spectra for 15 MeV electrons on tungsten and for ^{252}Cf fission neutrons; these are indeed seen to be quite similar.
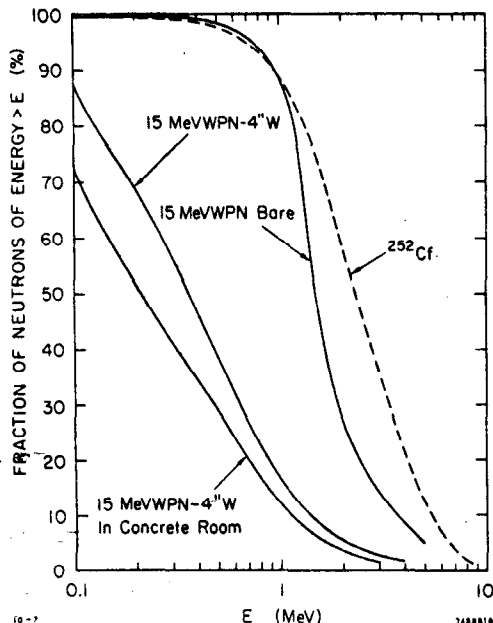

Fig. 5. Comparison of various neutron integral spectra to illustrate spectral modification by W shielding and a concrete room. The median energy can be reduced from 1.5 to about 0.2 MeV by the combined effects of the W and concrete. The bare ^{252}Cf spectrum is shown for comparison. Data are from the Monte-Carlo program MORSE.

On the same figure, we show the spectrum from 15 MeV electrons on tungsten after the neutrons have penetrated 10 cm of tungsten. It is clear that there is a large difference between these spectra. In particular, one can see that if one measures the neutrons from a 15 MeV medical accelerator, using a threshold detector calibrated with a bare ^{252}Cf source, the results will be considerably off. Also shown on this figure is the further degradation due to the concrete room in which medical accelerators are commonly placed. This will be discussed in a later section. In MJS a method was described of measuring accelerator leakage by measuring neutron fluence at various points in the room and using MORSE to simulate the room and the accelerator and to provide factors for converting the fluence measurements to dose equivalent or absorbed dose. Since this method requires the use of a computer and the availability of the MORSE program, MJS also developed a "cookbook" method using graphs and tables to provide the same conversion factors for fluence measurements.

Neutron Transport in a Concrete Room

Nearly every medical accelerator is placed in a concrete treatment room. In such a room, neutrons from the accelerator scatter in the concrete and may be absorbed or scattered back into the room. These neutrons add to the neutron field coming directly from the accelerator head. MJS investigated this scattered neutron field in order to evaluate their fluence measurements. Some time ago, Patterson and Wallace[10] discovered that if a fast neutron source is placed in a concrete room, a thermal fluence is produced which is approximately uniform over the entire room and is related to the fast neutron source strength by

$$\phi = k(Q/S)$$

where

ϕ = Thermal neutron fluence, Q is the fast neutron source strength, S is the inside surface area of the room, and k is a dimensionless constant.

Since the thermal neutrons represent a single point of the wall-scattered neutron spectrum, it was suspected that a similar relationship might hold for the entire wall-scattered spectrum. By a series of simulations using MORSE, this was found to be true; exactly the same relationship was found as for thermals but with a different constant coefficient. Measurements in MJS indicated that the scattered neutrons were indeed constant throughout the room. These wall-scattered neutrons are of quite low energy; this can be inferred from the lowest curve on the preceding figure which shows the effect of the walls of a typical therapy-sized room on the neutron spectrum. MJS found that the average energy of the scattered neutron spectrum was proportional to the average energy of the direct spectrum as shown in Fig. 6.[6] The fluence of the scattered spectrum is given in the following equation:

$$\phi = k_1(Q/S)$$

From MORSE we found that k_1 is equal to 4.6 for the tungsten-shielded machines and 5.4 for lead-shielded accelerators. The values of k_1 are different since there is no attenuation of the fluence in practical thicknesses of lead, and a transmission of about 0.85 in typical thicknesses of tungsten. This relationship enables one to correct calculated or measured values of the direct fluence for a particular room. The wall-scattered component often makes a significant contribution (20-30%) to the measured neutron fluence. However its contribution to the patient's integral dose is a much smaller fraction of the total, because of the softening of the scattered spectrum discussed above (Fig. 6).

It should be noted that the original paper by Patterson and Wallace enables one to calculate the fast neutron source strength in a room of normal concrete simply by measuring the thermal neutron fluence at any point in that room. This method works quite well. The variation in the thermal neutron capture in normal concretes
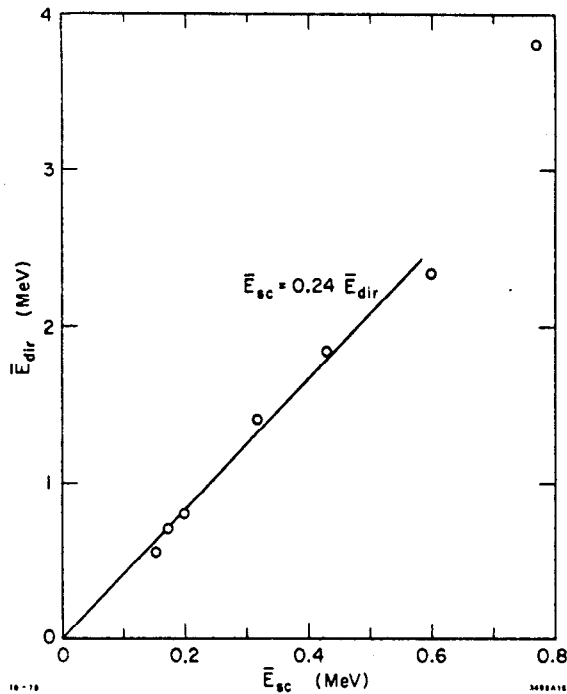
Fig. 6. Comparison of the average energy of source spectra and neutrons scattered from a concrete room within which the source is placed. The straight line illustrates the close proportionality of these average energies.

Fig. 7. Arrangement of neutron-producing parts within a radiation treatment unit (not to scale). All of these components are practically indispensible and are found on all standard models. Numbers indicate the approximate percentages of neutrons produced at 25 MeV relative to the maximum number possible, assuming all parts are of high-Z materials (W or Pb).

does not vary enough to cause a large error. It should be noted however, that if the room is built of heavy concrete such as ilmenite or barite concrete, the thermal neutron capture cross sections are considerably larger than in normal concrete, and the method will then underestimate the source strength. In such cases, there is enough variation in the various heavy concretes that one would have to make a calibration of each room by putting, for example, a PuBe source in the room and measuring the thermal fluence and redetermining the constant in the equation, then using this constant in evaluating the thermal neutron measurements with the accelerator operating.

Neutron Production in a Medical Accelerator

From Swanson's[15,16] calculations, one can calculate the neutron yield from a single target material of finite or infinite thickness ($\gtrsim 10$ R.L.). It is of interest to compare the neutron yield from an accelerator with these models.

We will consider a typical therapy machine with the geometry of Fig. 7.

Case 1. Target, Flattener, Jaws and Shielding All of the Same Material

This would always be Pb or W and, to a reasonable approximation, the n yield of these can be considered the same. The only photons effective in producing neutrons are those above about 8 MeV. These are mostly forward directed and will either be absorbed in the main collimator or pass through
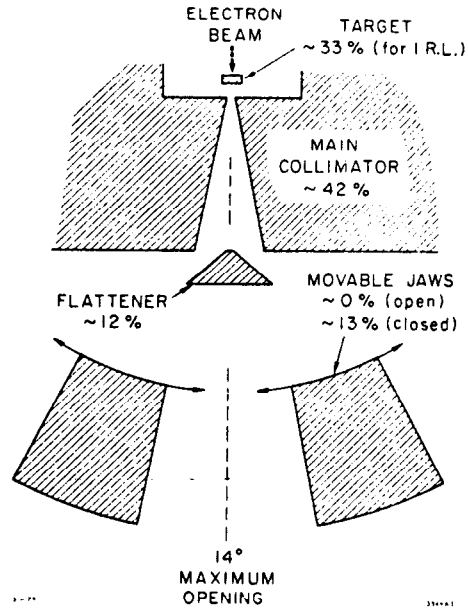
its opening and through the flattener. Those which penetrate the flattener may or may not strike the jaws, depending on their opening. Those passing through the jaws' opening may be absorbed in the patient, the beam stopper if there is one, or the room concrete. The neutron yield from concrete can be considered negligible, especially since self-shielding would be large. We then have the following possibilities:

Case 1a – Jaws closed – Yield will be that of an infinite target;

Case 1b – Beam stop in place – Yield will be that of an infinite target;

Case 1c – No beam stop in place – Yield will depend on position of jaws.

Cases 1a and 1b provide upper limits to the amount of neutron production. Case 1c is more complicated and we will consider it in more detail. Most medical linacs provide fields up to about 35×35 cm^2 at 100 cm from the target. The main collimator covers all forward directions beyond the extremes of these fields. The half-angle of the main collimator is then about 14 degrees. In order to see what fraction of the high-energy (> 8 MeV) photons are within this angle we have used the Monte Carlo program EGS[3] for various target thicknesses and electron energies. We have used what we believe to be practical linear accelerator target thicknesses. At these thicknesses,

about 2% of the incident electron energy is transmitted by electrons in the cone within 14°. Since the average energy of these transmitted electrons has been reduced sharply, the radiation yield will be low and there should be no penumbra problems from bremsstrahlung produced in the flattener or elsewhere. The target thicknesses we have considered are listed in Table II.

Table II. Target Thicknesses Considered

Electron Energy (MeV)	Target Thickness (R.L.)	
	Copper	Tungsten
14	0.3	0.7
20	0.4	0.85
25	0.74	1.00
30		1.1
35	0.92	
45	1.05	

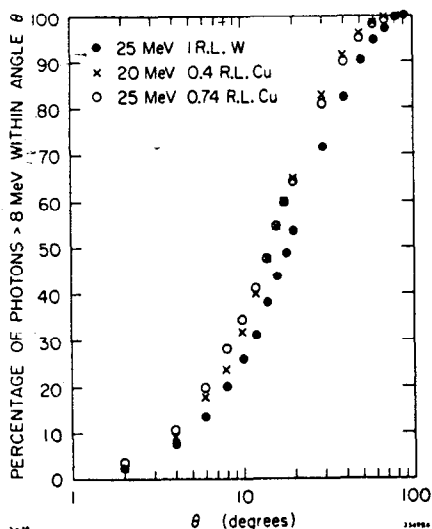From our Monte-Carlo calculation we can construct curves such as are shown in Fig. 8.

Fig. 8. Percentage of high energy photons (> 8 MeV) emitted within the angle θ from an accelerator target, as a function of θ. Three target material and thickness combinations are shown. Data are based on Monte-Carlo calculations using the program EGS.

As a calculational example consider a 25 MeV accelerator with a 1.0 R.L. W target, W head shielding and a W flattener. From Fig. 10 of Swanson,[15] we find that the neutron yield from this target is about 33% of that from an infinite target. From Fig. 8 we see that the remaining high-energy photons are 38% inside the main

collimator angle and 62% outside, and these strike the main collimator which is practically an infinite absorber. The 38% inside the main collimator strike only the flattener. A tungsten flattener for this target would be about 2.3 cm (6.6 R.L.) thick in the center and approximately conical. If we weight this conical shape with the high-energy photon distribution, we effectively have 2.9 R.L. over this angular range. Using Fig. 10 of Swanson again we find that these photons produce 47% of the infinite target yield (difference between 1 R.L. and $1 + 2.9 = 3.9$ R.L.). Our total neutron yield relative to the infinite target then is as follows:

Target	-	= 33%
Main Collimator	- $0.61 \times 67\%$	= 41.5%
Flattener	- $0.47 \times 0.38 \times 0.67$	= 12%
Total -		= 86.5%

From Fig. 8 of Swanson,[16] the yield for an infinite target of W at 25 MeV would be 1.5×10^{12} n/sec per kW. In Fig. 9 we have plotted the Monte-Carlo unflattened and flattened photon dose rates at a typical 1 meter target distance per mA of electron current for the target thicknesses of Table II.
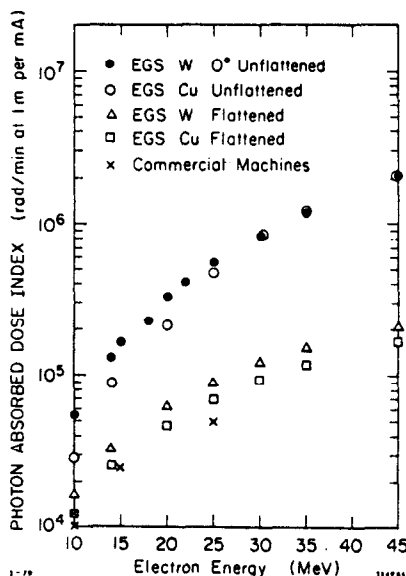

Fig. 9. Photon absorbed dose index as a function of incident electron energy, as obtained from the Monte-Carlo program EGS. Upper data are from W and Cu targets without flattener. Lower points show same data but after flattening. Measured values obtained on existing commercial accelerators are shown for comparison.

From this figure we have 8.95×10^4 rads/min per mA or 60 rads/sec per kW for our example. Then the yield of neutrons relative to the photon output would be 1.5×10^{12} n/sec-kW $\times 0.865 \div 60$ rads/sec-kW = 2.16×10^{10} neutrons/rad. This would be

the yield with the jaws fully open. Fully closed the yield would be $2.16/0.865 \times 10^{10} = 2.5 \times 10^{10}$ n/rad. With intermediate jaw openings the yield can be calculated by converting the jaw opening to angle and using Fig. 8 to calculate the yield.

Case 2. Target, Flattener, Jaws and Shielding of Different Materials

In all cases, the jaws and shielding will be of Pb or W, (the only other possible shielding material, depleted uranium, becomes activated due to photofission at energies too low to have significant photoneutron production). There are actually relatively few choices for the other elements. The required physical properties of the target limit the possibilities to copper, tungsten, gold, tantalum, platinum and silver. Tungsten, gold, tantalum and platinium are nearly identical in neutron production. The authors know of no example of silver being used. Therefore, we can limit the discussion of target material to copper and tungsten. Flatteners have been made of lead, tungsten and iron. Aluminum flatteners have been used in betatrons and proposed for linacs,[11,12] but are too long for rotational therapy machines and produce undesirable changes in beam hardness across the field.[7] In calculating neutron production then, it is sufficient to consider only iron and tungsten for the field flattener. We must finally consider the following cases.

> Case 2a - W target and shielding with an Fe flattener;
>
> Case 2b - Cu target and W shielding and flattener;
>
> Case 2c - Cu target, W shielding and Fe flattener..

Case 2a is not too different from our previous example. The neutron components from the target and the main collimator are the same. An iron flattener for 25 MeV would be about 9.4 cm = 5.3 R.L. long. If we assume that the spectral difference between the bremsstrahlung produced in a Cu and a tungsten target is insignificant we can proceed as before. The effective thickness of the flattener is 2.4 R.L. The photons striking the flattener produce 42% of the infinite target yield (difference between 1 R.L. and $1.0 + 2.4$ R.L. from Fig. 10 of Ref. [15]). The flattener neutron yield is given by $0.42 \times 0.38 \times 0.67 \times$ Fe yield/ W yield = 1.6% of the infinite W yield. The total yield for this machine would be 75.9% of the infinite tungsten target or 1.6×10^{10} n/rad with the jaws open.

Case 2b. It is easier to consider this case as relative to an infinite copper target. In the same manner as before we find the following:

> 0.74 R.L. Cu Target Yield - 25% of infinite (Fig. 10 of Ref. [15])
>
> Fraction of High-Energy Photons Passing through Main Collimator - 47.5% (from Fig. 8)
>
> Effective Flattener Thickness = 3.3 R.L.
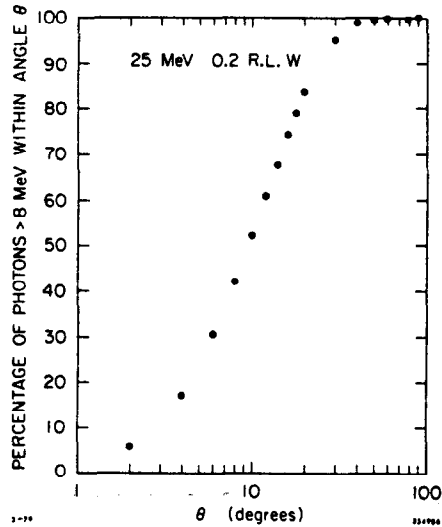>
> Infinite Target Cu Yield = 0.36×10^{12} n/sec-kW

Fig. 10. Percentage of high-energy photons (> 8 MeV) emitted within the angle θ, as a function of θ, when 25 MeV electrons are incident on an 0.2 R.L. W target. Data are from the Monte-Carlo program EGS.

Infinite Target W yield = 1.5×10^{12} n/sec-kW

Target Yield = 25% of Infinite Cu Target Yield

Flattener Yield = $0.55 \times 0.75 \times 0.475 \times 1.5$ × W Yield/Cu Yield
= 82% of Infinite Cu Target Yield

Main Collimator Yield = $0.525 \times 0.75 \times 1.5$ × W Yield/Cu Yield
= 164% of Infinite Cu Target Yield

Total: = 271% of Infinite Cu Target Yield
= 9.76×10^{11} n/sec-kW

The flattened dose rate from the machine would be 6.95×10^{4} rads/min at 1 meter for 1 mA. Then the relative neutron yield would be = 2.11×10^{10} n/rad.

Case 2c. This case is the same except that the neutron yield from the flattener has an effective thickness of 3.0 R.L. The infinite target yield for Fe is 0.23×10^{12} n/sec-kW.

Flattener Yield = $0.50 \times 0.475 \times 0.75$ × Fe Yield/Cu Yield
= 11.4% of Infinite Cu Yield

Total Yield = 200% of Infinite Cu Yield
= 7.2×10^{11} n/sec-kW

Since the flattened dose rate would be the same, the relative neutron yield would be 1.56×10^{10} n/rad.

The results of these calculations are summarized in Table III below.

Table III. Summary of Neutron Source Calculations (25 MeV electrons)

Target	Flattener	Main Collimator	n/rad	Fraction of Infinite W Yield (Percent)	Percentage From		
					Target	Flattener	Main Collimator
W	W	W	2.2×10^{10}	86.5	38	14	48
W	Fe	W	1.6×10^{10}	64	43	2	55
Cu	W	W	2.1×10^{10}	84	9.2	30	60.5
Cu	W	W	1.6×10^{10}	64	12.5	5.7	82

Note that while the total neutron yield does not change very much the fraction of the neutrons originating in different areas changes. This is useful information for an accelerator designer trying to minimize neutron production.

It is of some interest to compare the above results with those calculated for a 25 MeV betatron. The effective target thickness for a betatron is difficult to obtain since it is never known exactly where the electrons strike the target. However, we can get some indication from the angular distribution of the unflattened beam. ATC Betatron Corp, gives a graph of this in their literature.[1] The target is platinum which is very similar to tungsten. An EGS calculation for angular distribution of bremsstrahlung from a 0.2 R.L. W target matches the ATC graph quite well. Information kindly supplied by ATC indicates the electrons strike a nearly triangular target with a minimum thickness of 0.08 R.L. and a maximum thickness of 0.27 R.L. so assuming an effective target thickness of 0.2 R.L. seems quite reasonable. In this betatron the flattener is aluminum and the maximum field size is 14×14 cm^2 at 1 meter. The corner of this field would be at an angle of 5.7 degrees. The main shielding and jaws are lead. From Swanson[15] and interpolated results of Seltzer and Berger,[13] the neutron yield from the target would be about 3% of an infinite target. The angular distribution of the photons above 8 MeV is shown in Fig. 3. We can see that 29% of these photons are within 5.7 degrees. These photons strike only the aluminum flattener. The Al to W yield ratio is about 3.1% so the yield from the Al flattener is negligible. The 71% of the high-energy photons striking the main collimator give $0.71 \times 0.97 = 69\%$ of the infinite target yield; the total yield will be 72% of the infinite target yield or 1.08×10^{12} sec^{-1} kW^{-1}. The photon dose rate flattened to 5.7 degrees, 1 m from this target would be about 2.4×10^5 rads/min-mA and the relative neutron yield would therefore be 6.8×10^9 n/rad.

One might ask what happens to the electrons transmitted through this target. From the EGS calculation one can find that essentially all of the electrons are transmitted and carry an average energy of 19.6 MeV. Presumably, a few of these lose so little energy that they make another revolution and strike the target a second time. Most of the electrons, however, must spiral in and strike the donut. They would produce bremsstrahlung which would make neutrons but would not add to the useful photon yield. The neutron production from these electrons is difficult to estimate but because (1) the photon production is in low Z material, (2) the energy is lower, and (3) the neutron production would be partly in iron and copper rather than lead, it seems that these neutrons would add not more than 10% to the total.

We have made calculations similar to the above for several accelerators for which we have sufficient data on the geometry and materials. In each case, we made measurements of the total fast-neutron source strength (determined by the method described previously of measuring thermal neutrons in the room) and we have compared our results with these.* The results of these calculations are shown in the Table IV. In general, the comparison is fairly good. One should remember that we are comparing only the neutrons produced by electrons which produce the usable photon dose. In most machines, there are other electrons which are accelerated and lost, and these can contribute to the neutron leakage dose but not to the useful photon dose. It is believed that this is the largest part of the discrepancy for both models of the Clinac 35. This machine has two bends with energy analyzing slits before the beam strikes the target, and the authors suspect that there is a large beam loss at one or both of those bends. Both the Clinac 18 and the Mevatron XX would be expected to have a much smaller beam loss. These results indicate that, in accelerators where the beam losses are reasonably well-known and if target thicknesses and geometries are known, one can probably calculate the neutron yield per photon rad to within ±20%. With these calculations and the "cookbook" methods described in MJS, one could also calculate the head leakage for medical accelerators. The total accuracy one would expect should be no worse than about ±50%.

Accelerator	Energy (MeV)	Relative Neutron Yield (n/rad)	
		(Calculated)	(Measured)
ATC 25 MeV Betatron	25	6.8×10^9	6.9×10^9
Siemens 42 MeV Betatron	42	3.8×10^9	3.7×10^9
Varian Clinac 35 (Old)	25	4.3×10^{10}	8.1×10^{10}
Varian Clinac 35 (New)	25	2.2×10^{10}	6.2×10^{10}
Varian Clinac 18	10	3.9×10^8	4.2×10^8
Siemens Mevatron XX	15	5.8×10^9	7.6×10^9

Table IV. Calculated and Measured Neutron Yield per Photon Rad

Leakage Neutron Depth-Dose Curves

There has not been very much attention paid to the depth-dose distribution of the leakage neutrons in a patient. It has been shown that these neutrons are of very low energy, and one would expect them to be attenuated quite rapidly in tissue. We have made an attempt to calculate this depth-dose distribution using the computer code MORSE. In the calculation, we have assumed a point source 1 m from the center of the phantom. The source spectrum used was that of either a 14 MeV (incident electron energy) photoneutron spectrum surrounded by 4 inches of tungsten, or a 25 MeV photoneutron spectrum surrounded by 4 inches of tungsten. The phantom was a water cylinder one meter long and thirty centimeters in diameter, centered at 1 m from the target perpendicularly to the beam axis. In Fig. 11, we show the results of these calculations of absorbed dose for the two spectra. In Fig. 12, we show the dose-equivalent calculations for the same two spectra, using the ICRP-21 conversion factors (see Fig. 2). There are several things of interest in these two figures. First, it can be seen that there is a quality factor of about 10 throughout the depth of the phantom for both spectra. Second, it can be seen that the attenuation is quite sharp, so that there would be very little dose to the patient beyond 10 centimeters. Because of the large difference in penetration between these low-energy neutrons and the high-energy photon leakage, the integral dose-equivalent to the patient would be much less from the neutrons than from the photons, for the same dose-equivalent. In the calculations just presented, the radiation source and phantom were both in vacuum rather than in a concrete room. If the same calculation were done for a concrete room, a portion of the leakage dose to which the patient would be subjected would be the scattered component from the walls which would be much softer than the direct leakage spectrum. Therefore the attenuation of the scattered component would be much faster.

Figure 13 shows the calculated neutron fluence rate at 1 m per mA of incident electron current, plotted as a function of electron energy (from Fig. 5 of Ref. [16]). The conditions for which these curves hold correspond to the case in which all neutron-producing parts (Fig. 7) are of W or
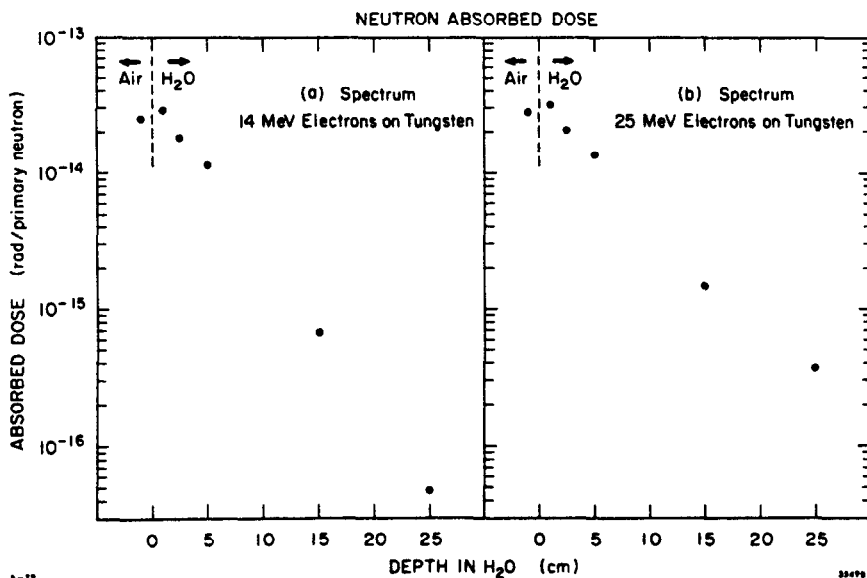

NEUTRON ABSORBED DOSE

(a) Spectrum 14 MeV Electrons on Tungsten

(b) Spectrum 25 MeV Electrons on Tungsten

ABSORBED DOSE (rad/primary neutron)

DEPTH IN H_2O (cm)

Fig. 11. Absolute depth-dose distributions in H_2O for neutron spectra from therapy targets, modified by 10 cm of W. The water phantom is a 30 cm-diameter cylinder, 2 m long, oriented perpendicularly to the beam axis and centered at 1 m from target. Units are rads per primary (photo-) neutron. The air-water interface is indicated at 0 cm (the leftmost point represents the air dose). Data are from the Monte-Carlo program MORSE.
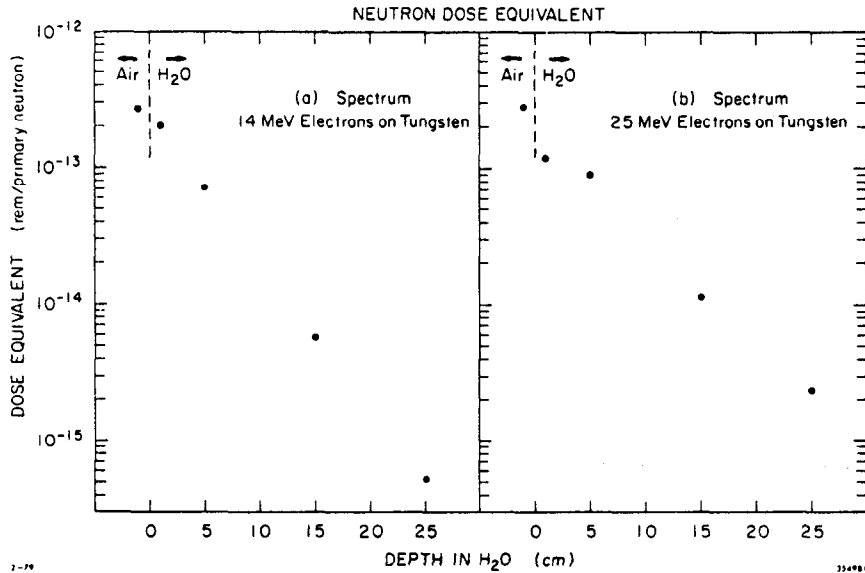(a) 14 MeV incident electrons;
(b) 25 MeV incident electrons.

NEUTRON DOSE EQUIVALENT

Fig. 12. Absolute depth-dose-equivalent distributions in H_2O for neutron spectra from therapy targets modified by 10 cm of W. Conditions are the same as for Fig. 11, except units are rem per primary neutron.
(a) 14 MeV incident electrons;
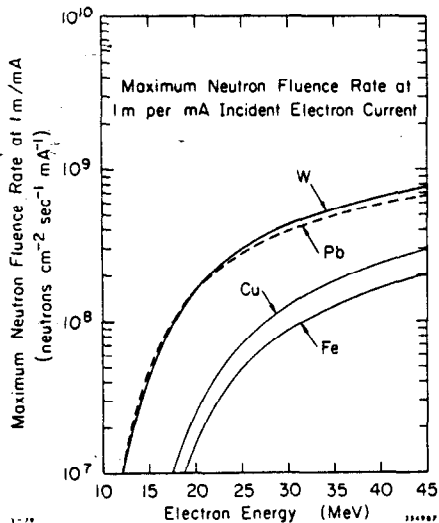(b) 25 MeV incident electrons.

Fig. 13. Calculated maximum neutron fluence rate at 1 m per mA of incident electron current, plotted as a function of electron energy. The conditions for which these curves hold correspond to the case in which all neutron-producing parts (Fig. 7) are of W or Pb and the movable jaws are fully closed. Isotropic neutron production and no attenuation of neutrons in shielding materials are implicitly assumed. Lower two curves correspond to cases in which all neutron-producing parts are made of Fe or Cu and are shown for comparison. Data are derived from Fig. 5 of Ref. [16].

Pb and the movable jaws are fully closed or almost so. Note that the contribution of the movable jaws would amount to about 13% of the total (at 25 MeV; see examples above). Isotropic production of photoneutrons is implicitly assumed. For this graph we also neglect the attenuation of neutron fluence in high-Z shielding as well as the room-scattered component discussed above. The high-Z materials would change the fluence by a factor in the range 0.85 (for W) to 1.0 (Pb). The room-scattered component would boost the fluence by about 20% but increase the patient's integral dose by a relatively smaller amount. As these effects are not large and tend to cancel, we believe that the curves of Fig. 13 reliably represent the maximum neutron fluence of significance to the patient, assuming that the electron beam only strikes the intended target.

The result of dividing the data of Fig. 13 by those of Fig. 9 gives us the ratio of the maximum neutron fluence ϕ_{max} to the useful photon dose at the same distance. This is an absolute prediction to which comparison with measurement is invited. This ratio becomes nearly constant above about 25 MeV incident electron energy where its value is about 2.1×10^5 neutrons cm^{-2} rad^{-1}. As discussed by examples above, measured data that fall significantly below the curve are likely due to cases in which energy-absorbing accelerator components are not all of high-Z materials, or measurements were made with the movable jaws open. Points that fall significantly above probably represent cases in which there is substantial loss of beam on "targets" within the transport system before it reaches the intended target.

Using the above information, we are in a position to compare numerically the integral dose from neutrons to the integral dose from leakage photons. For the numerator of our comparison we integrate the curves of Fig. 11 over the range 0–30 cm and multiply by the strength of the neutron source per photon treatment dose (from Fig. 14). For the denominator we integrate an exponential
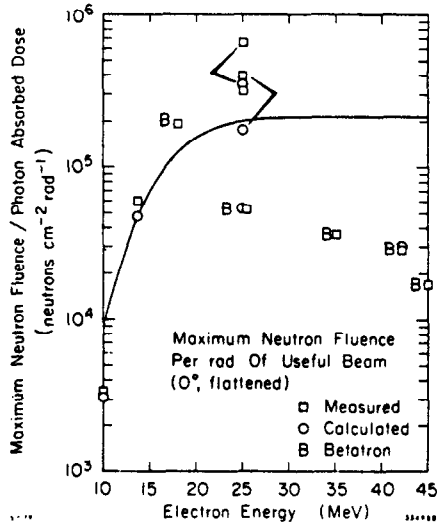
Fig. 14. Maximum neutron fluence
per rad of useful beam 0°, flattened).
Data are from the W curve of Fig. 13,
divided by the photon absorbed dose
index for W (flattened) as calculated
by the Monte-Carlo program EGS (the
triangles of Fig. 9). The conditions
for which this curve holds are the
same as for Fig. 13. Calculated
points (circles) and measured points
(squares) are mostly from Table IV.

over the same interval 0-30 cm, using -0.041 and
-0.037 cm^{-1} as values of the attenuation coeffici-
ent for 14 and 25 MeV, respectively. The attenua-
tion of the photon distributions includes the
inverse-square reduction with distance, as is the
case for the neutron distributions (Fig. 11). The
denominator is multiplied by 0.001, corresponding
to the ratio of leakage radiation to useful beam
found in most standard accelerator models. This
is meant only to be a rough comparison and details
of the phantom geometry are neglected. The results
are:

$$\frac{\text{neutron integral absorbed dose}}{\text{leakage photon integral absorbed dose}}$$

- 0.04 (at 14 MeV), and

- 0.20 (at 25 MeV).

Using the quality factor estimated by comparison
of Figs. 11 and 12, we would multiply by $\bar{Q} = 10$ to
obtain

$$\frac{\text{neutron integral dose-equivalent}}{\text{leakage photon dose-equivalent}}$$

- 0.4 (at 14 MeV), and

- 2.0 (at 25 MeV).

We note that most of the difference between these
two energies is directly traceable to the increase
in neutron yield per useful photon dose seen in
Fig. 14.

Conclusions

Based on what we consider quite reasonable
models, we can make the following statements re-
garding neutron sources and their characteristics:

(a) We have identified the significant sources of
neutrons within the treatment head, and given
absolute estimates of the amount of neutron
fluence per treatment dose for various
choices of target.

(b) MORSE calculations show that the neutron
fluence is nearly unaffected by transport in
the high-Z shielding contained in standard
treatment units.

(c) On the other hand, the same calculations show
that the neutron spectrum is softened signi-
ficantly by transport by the high-Z material.

(d) We have considered the component of neutrons
scattered by the concrete room and found its
average energy to be about 0.24 of the primary
source average energy. The scattered com-
ponent can make a significant contribution to
fluence measurements (about 20%), but con-
siderably less to the patient's integral dose.

(e) We have submitted an absolute prediction of
the ratio of neutron fluence (at 1 m) to the
useful photon dose at the same distance.
This ratio rises to an approximately constant
value of 2.1×10^5 neutrons cm^{-2} rad^{-1} at
incident electron energies above 25 MeV.

(f) Measurements at a variety of linear accelera-
tor installations fall within a factor of
three of this curve. We suggest that signi-
ficant deviations of correct measurements can
be explained by (1) use of materials other
than high-Z within the treatment head (if the
data fall below), or, (2) partial loss of the
electron beam before it strikes the target
(if above).

(g) The neutron fluence from betatrons is sub-
stantially below that from linear accelerators.
The reasons are twofold: (1) Because most of
the energy of the electron beam is expended
in the low-Z material of the donut, there is
smaller neutron production per incident elec-
tron beam current. (2) Because the smaller
treatment fields permit a thinner flattener
there is higher photon output per incident
electron beam current.

(h) By means of MORSE, we have calculated absolute
depth-dose and depth-dose-equivalent distri-
butions for realistic neutron spectra in H_2O
phantoms and found a rapid falloff with depth.

(i) Using the neutron depth dose curves presented
in this work, together with the estimate of
neutron fluence, we are able to calculate the
ratio of neutron integral absorbed dose to
leakage photon absorbed dose. These values
are 0.04 and 0.2 for 14 and 25 MeV incident
electron energy, respectively. If a quality
factor $\bar{Q} = 10$ is applied, these correspond to
0.4 and 2.0 neutron integral dose-equivalent
per leakage photon integral dose-equivalent.

(j) As for reducing the neutron fluence per useful photon dose, the following remarks may be made: (1) As the effective use of these machines for photon therapy depends on the use of high-Z materials to produce intense, wide fields with sharp edges, the possible reduction in neutron production is not very great. Thinner targets would be of some help, and certainly most of the neutron production by electrons striking parts of the transport system can be eliminated by improved design or lower-Z materials at critical points. Other than these steps, the only alternative is to treat patients at lower energies where possible. There is a factor of two reduction from the maximum in neutron production per treatment dose at about 17 MeV and a steep drop as the energy is reduced further.

Acknowledgement

The authors wish to express their appreciation to R. A. Shore for his help in doing computer calculations.

References

[1] ATC Betatron Corporation, Twenty-Five Million Volt Betatron for Radiation Therapy, P. O. Box Drawer 14248T, West Allis, WI 53214 (1974).

[2] B. L. Berman, "Atlas of Photoneutron Cross Sections Obtained with Monoenergetic Photons," Bicentennial Edition, Lawrence Livermore Lab, Report No. UCRL-78482 (1976). Also see "Atlas of Photoneutron Cross Sections Obtained with Monoenergetic Photons," Atom. Data Nucl. Data Tables 15, 319 (1975).

[3] R. L. Ford and W. R. Nelson, "The EGS Code System: Computer Programs for the Monte-Carlo Simulation of Electromagnetic Cascade Showers (Version 3)," Stanford Linear Accelerator Center, Stanford, CA, Report No. SLAC-210 (1978).

[4] R. J. Howerton, "An Integrated System for Production of Neutronics and Photonics Calculational Constants," Lawrence Livermore Lab, Report No. UCRL-50400, Vol. 9 (1970).

[5] International Commission on Radiological Protection, "Data for Protection Against Ionizing Radiation from External Sources:" Supplement to ICRP Publication 15, ICRP Publication No. 21, Table 9, p. 19 (1973). (Oxford: Pergamon Press.)

[6] R. C. McCall, T. M. Jenkins and R. A. Shore, "Transport of Accelerator Produced Neutrons in a Concrete Room," paper presented at the 5th Conference on Applications of Small Accelerators, held at North Texas State University, Denton, TX, November 6-8, 1978, Stanford Linear Accelerator Center, Stanford, CA, Report No. SLAC-PUB-2214 (1978).

[7] R. C. McCall, R. D. McIntyre and W. G. Turnbull, "Improvement of Linear Accelerator Depth-Dose Curves," Med. Phys. 5, 518 (1978).

[8] G. S. Mutchler, "The Angular Distributions and Energy Spectra of Photoneutrons from Heavy Elements," Ph.D. Thesis, MIT, Report No. MIT-2098-224 (1966).

[9] National Bureau of Standards, National Council on Radiation Protection and Measurements, "Shielding for High-Energy Electron Accelerator Installations," NBS Handbook No. 97 and NCRP Report No. 31, Washington, D.C., Fig. 15, p. 25 (1964).

[10] H. W. Patterson and R. Wallace, "A Method of Calibrating Slow Neutron Detectors," Lawrence Berkeley Lab, Berkeley, CA, Report No. UCRL-8359 (1958).

[11] E. B. Podgorsak, J. A. Rawlinson, M. I. Glavinovic and H. E. Johns, "Design of X-Ray Targets for High Energy Linear Accelerators in Radiotherapy," Am. J. Roentgenol. Rad. Therapy Nucl. Med. 121, 873 (1974).

[12] E. B. Podgorsak, J. A. Rawlinson and H. E. Johns, "X-Ray Depth-Doses from Linear Accelerators in the Energy Range from 10 to 32 MeV," Am. J. Roentgenol. Rad. Therapy Nucl. Med. 123, 182 (1975).

[13] S. M. Seltzer and M. J. Berger, "Photoneutron Production in Thick Targets," Phys. Rev. C7, 858 (1973).

[14] E. A. Straker, P. N. Stevens, C. C. Irving and V. R. Cain, "The MORSE Code - A Multigroup Neutron and Gamma-Ray Monte-Carlo Transport Code," Oak Ridge National Lab, Oak Ridge, TN, Report No. ORNL-4585 (1970). Also see Radiation Shielding Information Center, RSIC Computer Code Collection, "MORSE-CG, General Purpose Monte-Carlo Multigroup Neutron and Gamma-Ray Transport Code with Combinatorial Geometry," Radiation Shielding Information Center, Oak Ridge, TN, Report No. CCC-203 (1976).

[15] W. P. Swanson, "Calculation of Neutron Yields Released by Electrons Incident on Selected Materials," Stanford Linear Accelerator Center, Stanford, CA, Report No. SLAC-PUB-2042; and Health Phys. 35, 353 (1978).

[16] W. P. Swanson, "Calculation of Neutron Yields Released by Electrons near the Photoneutron Threshold," Stanford Linear Accelerator Center, Stanford, CA, Report No. SLAC-PUB-2211 (Rev. 1979); and Health Phys., to be published (1979).